



Evolution of L1₂ Ordered Precipitates in Cu–Fe–Si Alloy System and Its Influence on Potential Strength–Conductivity Properties

Suman Sarkar^{1,2} · Shyam Kanta Sinha¹ · Dhanalakshmi Palaniswamy¹ · Chandan Srivastava¹ · Kamanio Chattopadhyay¹

Received: 18 October 2022 / Revised: 22 January 2023 / Accepted: 1 February 2023 / Published online: 17 February 2023
© ASM International 2023

Abstract

We report a copper-based alloy strengthened by L1₂ ordered precipitates and exhibiting a strength of 370 MPa and thermal conductivity of 290 (W/m.K) at 400 °C. The alloy is based on a Cu–Fe–Si system with the optimum composition of Cu-2.5at%Fe-2.5at%Si and processed by the suction casting of the melt. The strengthening precipitates are crystallographically L1₂ ordered. The precipitates were evolved during post-solidification cooling and are coherent with continuous fcc copper matrix. Ordered precipitates show a cube-on-cube orientation relationship with the matrix. This feature promotes low interfacial energy and are useful for retaining high temperature strength. The composition of the precipitates was determined through 3D-APT studies and found to be ~Fe₆₈Cu₉Si₂₄ (at.%). The coherent nature of the order–disorder interface and the low solid solubility of iron in the copper matrix impart resistance to coarsening at high temperatures. The high strength at room temperature (~690 MPa) is attributed to the coherency strain around the uniformly dispersed precipitates. However, order hardening plays a significant role at higher temperatures as coherency strain decreases with temperature, evidenced by the loss of strain contrast in TEM images. The combination of the significant stability of the microstructure and high-temperature strength makes this alloy attractive for high heat flux application at elevated temperatures domain.

Keywords Alloy · Copper alloys · Suction casting · Rapid solidification · TEM · APT · Immiscibility · L1₂ order · Yield strength

Introduction

Copper and most Cu-based alloys exhibit good thermal and electrical conductivity. Hence, alloys with good strength at room and higher temperatures make this class of alloys attractive for various industrial applications. In particular, the materials for high heat flux applications, like liners for the combustion chamber of launch vehicles for space and other applications, require good high-temperature mechanical properties, superior thermal conductivity with robust oxidation and corrosion resistance at elevated temperatures. Besides high heat flux applications, high strength and high conductivity copper alloys are needed for non-sparking

tools, landing gears, lead frames, and electrical contacts. The above applications demand good mechanical strength, plasticity, and electrical conductivity [1–41].

In general, there is a trade-off between strength and conductivity due to the presence of defects. Hence, simultaneously achieving good high-temperature strength and thermal conductivity present a challenge. Several such alloys have recently been developed with reasonable success [1–15]. The strength of copper can be increased in several ways, including solid solution strengthening, cold working and grain refinement. However, adopting these routes reduces thermal conductivity significantly and hence, they have limited utility. Most of the high-strength high-conductivity copper-based alloys are developed by introducing fine-scale dispersions or precipitation in the copper matrix through alloying. Chromium is prominent among them, while newer alloys containing Zr, Fe, and Si are also being developed. Currently, efforts are being made to develop newer dispersion strengthened copper alloys utilizing oxides, carbides, and intermetallic compounds [22–41]. An active route is to utilize phosphorous with transition metals

✉ Suman Sarkar
suman.sarkar@iitjammu.ac.in

¹ Department of Materials Engineering, Indian Institute of Science, Bangalore 560012, India

² Department of Materials Engineering, Indian Institute of Technology Jammu, Jammu, India

like Fe and Mn, promoting the formation of fine phosphides during cooling. Internal oxidation was also popular in the early days of developing high-strength copper-based alloys [22–41]. The dispersion of carbides and silicide like TiC, nickel silicide, and intermetallic compounds is being attempted to develop strength at higher temperatures [24–26]. Dispersions can also be achieved by utilizing alloy systems that exhibit a miscibility gap with copper [15–21]. However, the strength of dispersion strengthened alloys is not as high as that obtainable through precipitation hardening. Many successful alloying additions that promote precipitation hardening in copper alloys are reported in the literature. The most prominent of these is Mg, Be and Ti [11, 22–25]. The most successful current alloys are based on copper, chromium and niobium with a nominal composition of Cu-8Cr4Nb [26–30]. This alloy has excellent high-temperature properties, high thermal conductivity at elevated temperatures, good strength, creep resistance, and resistance to corrosion. An atomization and compaction route are followed to manufacture this alloy, as a significant cooling rate is necessary to develop the desired microstructure.

We have recently reported a copper-based alloy suitable for applications like valve seat in IC engine that requires wear resistance and good heat dissipation capacity [15]. The alloy utilizes the miscibility gap in Cu–Fe–Si system to phase separate micron-size globules in the copper matrix. During this work, we observed coherent precipitates in the copper matrix. The observation led us to anticipate that it may be possible to use these precipitates to design a new high-strength copper alloy. Our subsequent investigation revealed that besides high strength at elevated temperatures, such an alloy exhibits enhanced thermal conductivity at high temperatures. This was an attractive observation for high heat-flux application. The present paper reports this effort.

The alloy studied in this work shows the strengthening of copper matrix by coherent $L1_2$ ordered precipitates. The coherent interface resists coarsening of the precipitates at high temperatures. The developed coherency strain between precipitates and Cu-matrix provides a good room temperature strength and excellent high-temperature properties due to the evolution of crystallographically ordered precipitates. The release of coherent interfacial strain with increasing temperatures is balanced by order hardening mechanism. This type of microstructural features helps in retaining the high-temperature strength and offers enhanced thermal conductivity.

Experimental Method

Alloy sample of nominal compositions, Cu-2.5at%Fe-2.5at%Si, was produced by melting the constituent elements under an argon environment using a vacuum arc melting unit with a water-cooled copper hearth and a tungsten electrode. They

were chill cast under an argon environment into 3 mm and 6 mm rods and 3-mm-thick slabs using copper mold connected to a vacuum suction casting machine. Table 1 shows the measured compositions of the bulk alloy sample. The composition was determined using a large area scan utilizing the wavelength dispersive spectrometer (EPMA-WDS) attached to the electron probe micro-analyzer (EPMA; JEOL). The heat treatments were carried out in a line-focused gold infra-red image furnace (ULVAC-RIKO.INC, Model: RHL-E44VHT, Power: AC200V 8 kW). A continuous flow of 95% Ar + 5% H₂ gas mixture was purged during the heating experiment to maintain a reducing atmosphere inside the furnace. Alloy samples were quenched directly in water after heat treatment. The hardness of the alloy samples was determined using a Vickers microhardness testing machine FM800 (Microhardness Tester, Future Tech Corp).

X-ray diffraction process was adopted to identify different phases present in the alloy samples using an X-ray diffractometer (X'Pert PRO system, PANalytical make). The test data were collected using Cu-K α radiation in the 2 θ range of 20°–140° with a step size of 0.03° and a scan speed of 0.006/s.

The newly synthesized alloy samples were characterized for microstructure and mechanical properties. The synthesized alloy samples' initial surface morphology and the fracture surface were studied using a scanning electron microscope (FEI ESEM Quanta 200 SEM). Finer details of the microstructure and spatial composition distribution across the interfaces of evolved phases were analyzed using a transmission electron microscope (TEM) equipped with a field emission source (F30 model, FEI). Both standard imaging with diffraction contrast and high-resolution TEM imaging was performed. TEM foils (specimens) were made by initial mechanical thinning (less than 100 microns) followed by milling with argon ion using a Gatan Ion-Mill machine (precision ion polishing system (PIPS)) operating at an accelerating voltage of 5 kV and 4°–2° incidence angle. The in situ heating method in the TEM was performed using a specially designed Gatan-make double tilt heating holder (Model 652. T.A.).

The distribution of the phases and their compositions was further evaluated by carrying out 3D atom probe tomography (3D APT) studies. Specimens for APT were prepared using

Table 1 Composition of the suction cast alloy determined by electron probe (WDS) microanalysis

Elements	Nominal composition, atom%	Overall measured alloy composition, atom%
Cu	95	94.8 ± 0.2
Fe	2.5	2.7 ± 0.2
Si	2.5	2.5 ± 0.1

a dual-beam focused-ion-beam instrument (FIB, FEI Helios 600) via an in situ lift-out mechanism [42, 43]. The APT analysis was done in a LEAP™ 5000 XR system (Cameca Instruments Inc., Madison, WI) capable of operating in a reflectron mechanism. Ultraviolet picosecond laser pulse at a repetition rate of 125 kHz and pulse energy of 40 pJ were set during APT analysis. Specimen's base temperature was maintained at 60 K during the analysis. The rate of detection was maintained as 5 ions detected per 1000 pulses throughout the experiment. IVAS™ 3.8.4 software package was used for data analysis.

The mechanical responses of the alloy samples were evaluated both at ambient and elevated temperature by tensile testing. The tensile specimens were tested using the INSTRON-5967 electromechanical testing machine. The sample geometrical dimensions are shown in Fig. 11c. The dimension of the specimens can be noted as 0.5 mm in thickness, 2 mm in width, and 6 mm in gauge length. The tensile specimens were prepared from 3 mm width suction cast slab strips by EDM cutting. The specimens were polished carefully by emery paper to obtain the desired thickness (Fig. 11c). The length to width ratio of all the samples is kept as 3 and comparable with ASTM E8 standard [67, 68]. Each test was performed on 5 samples with same alloy composition and dimension to achieve the best statistical data sets. The average tensile test results along with the statistical scattering (standard deviation) have been reported. A load cell with a capacity of 5 kN was used to conduct the tests. The tests were carried out at varying temperatures till 600 °C. Tests were done with 10^{-3} s^{-1} and 10^{-4} s^{-1} strain rates to observe the strain rate sensitivity of the alloy samples. The newly synthesized alloys did not reflect any strain rate sensitivity. All the reported test results of current study were performed with a strain rate of 10^{-3} s^{-1} .

The electrical resistivity measurements for all the alloys have been carried out using ULVAC-RIKOZEM-3 M10 instrument. This instrument allows the measurement of electrical resistance at different temperatures under a low-pressure helium gas environment. A four-probe terminal method has been used for electrical resistance determination. The samples of the known cross section were kept between two electrodes. The sample resistance value "R" was determined by measuring the current "I" set with the constant current power supply and the voltage.

The thermal conductivities are evaluated using TA Instruments FL5000 Thermal Properties Analyzer, which uses the laser flash method for property determination. The thermal conductivity can be measured from the thermal diffusivity data, specific heat capacity and density of the sample applying the following equation.

$$\kappa_{\text{total}} = \alpha C_p D,$$

in this equation, κ_{total} is the total thermal conductivity, α is the thermal diffusivity and C_p is the specific heat at constant

pressure. D denotes the density of the studied alloy sample. Tests were performed on five samples with the same alloy composition and dimension to achieve the best statistical data sets.

The Structure and Microstructure of Cu–Fe–Si Alloy

The quantitative composition analysis using EPMA-WDS representing the composition of our alloy is presented in Table 1. The X-ray diffraction pattern obtained from the suction cast Cu-2.5at%Fe-2.5at% Si alloy sample exhibits copper-rich matrix reflections. Figure 1 shows the two strongest copper solid solution reflections, 111 and 002. The 002 reflection has a weak shoulder toward a higher angle which on deconvolution shows a weak and broad peak as shown in the inset.

A representative SEM micrograph of the Cu-2.5at%Fe-2.5at% Si suction cast alloy sample taken in back scattered mode (BSE) is shown in supplementary Fig. S1. The cast microstructure reveals the existence of small amount of segregation inside the matrix. The WDS Mapping reveals that segregates are mainly rich in iron and silicon, whereas the matrix is rich in copper. The segregation can be linked with the immiscible nature of the iron.

Further details were obtained through a transmission electron microscope study. Figure 2 shows a set of electron diffraction patterns taken along 100, 110 and 111 zones with weak superlattice reflections corresponding to L_{12} ordering (γ'). The schematic of the indexing is included in Fig. 2. A (011) dark field image taken under two-beam condition reveals a uniform distribution of nanometer size precipitate particles within the Cu-rich matrix (Fig. 3c). A bright field

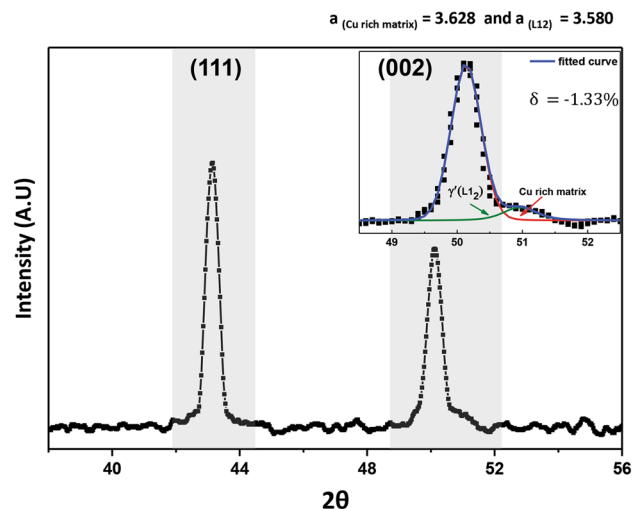


Fig. 1 A portion of the powder X-ray diffraction pattern of the suction cast Cu-2.5Fe-2.5Si alloy showing the fcc 111 and 002 reflections. The inset shows deconvolution of the 002 peak revealing the superlattice reflection of L_{12} ordered precipitates

image with slightly higher magnification is shown in Fig. 3b ($g=022$). Most of the particles show an Ashby–Brown line of no contrast due to the coherency strain field around the particles [44–46]. A few exceptions are those where diffraction condition is slightly deviated during imaging of the strain field contrast as can be noticed in Fig. 3b. The mean diameter of these nanometer-size precipitates is 12.3 ± 1.3 nm. Their size distribution is shown in Fig. 3d. Assuming the broad shoulder in the X-ray diffraction pattern originates from $L1_2$ ordered g' precipitates, the lattice parameter of the copper-rich matrix is 0.3628 nm, while that of γ' is smaller, 0.358 nm.

To reveal the composition of the precipitates, we have carried out STEM (Scanning-TEM) mapping of

composition. Figure 4a shows the STEM-HAADF (High Angle Annular Dark Field) image of the precipitates in the copper matrix. The spatial distribution of the elements in the ordered precipitates (Fig. 4b–d) reveals the nature of Cu, Fe, and Si partitioning across the precipitates and the surrounding Cu-rich matrix. Figure 4b–d confirms that these nanometer size $L1_2$ ordered precipitates are rich in Fe and Si and depleted in copper. Compositional mapping of silicon distribution (Fig. 4d) also indicates that some silicon may have partitioned in the copper matrix. An attempt to quantitatively estimate the composition of the precipitates by TEM was not successful because of the presence of the underlying copper matrix. We have, therefore, carried out 3D-APT studies.

Fig. 2 (a)–(c) Series of diffraction patterns, obtained by systematic tilting over a unit stereographic triangle in the copper matrix that establish the $L1_2$ Order Structure

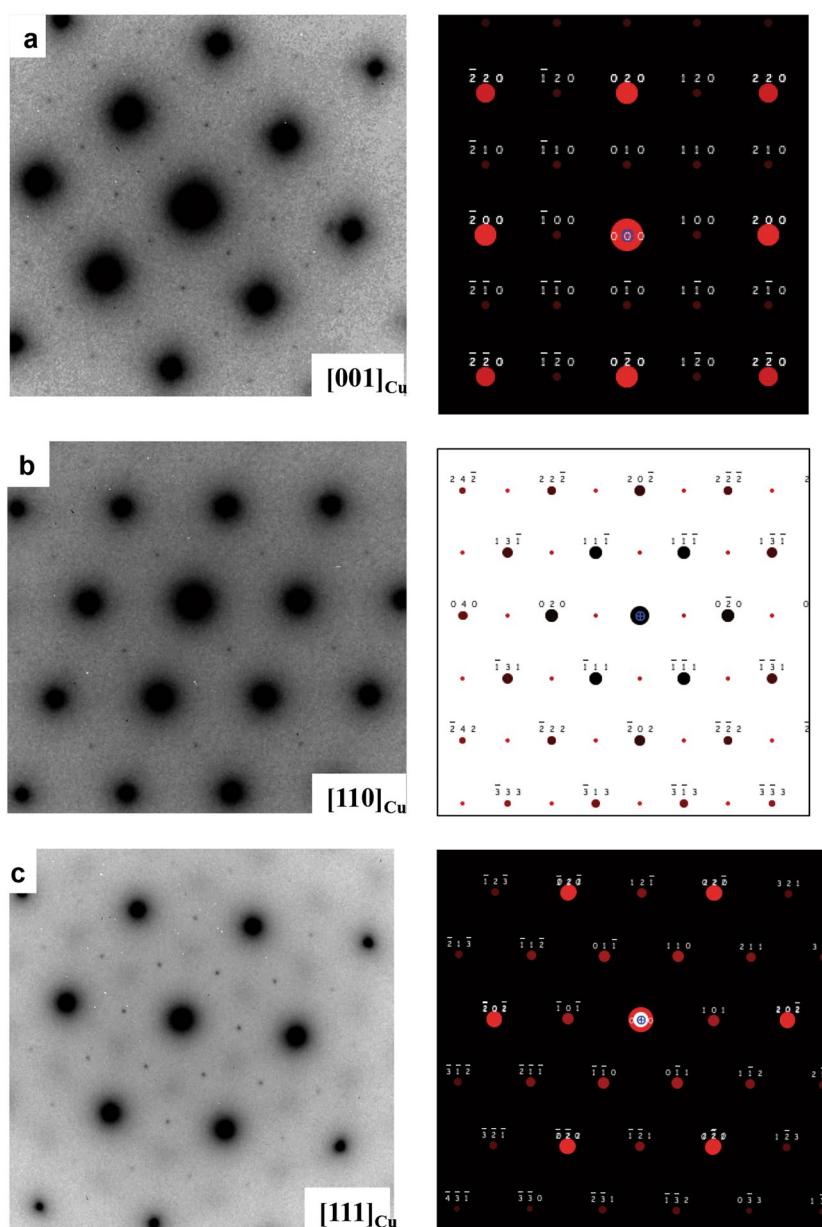


Fig. 3 (a) [211] zone axis SAD pattern and two-beam diffraction condition (inset) from the suction cast Cu-2.5Fe-2.5Si alloy. (b) A bright field micrograph showing the distribution of fine precipitates with large strain contrast. (c) Lower magnification darkfield image revealing the distribution of the nanoprecipitates (d) Particle size distribution

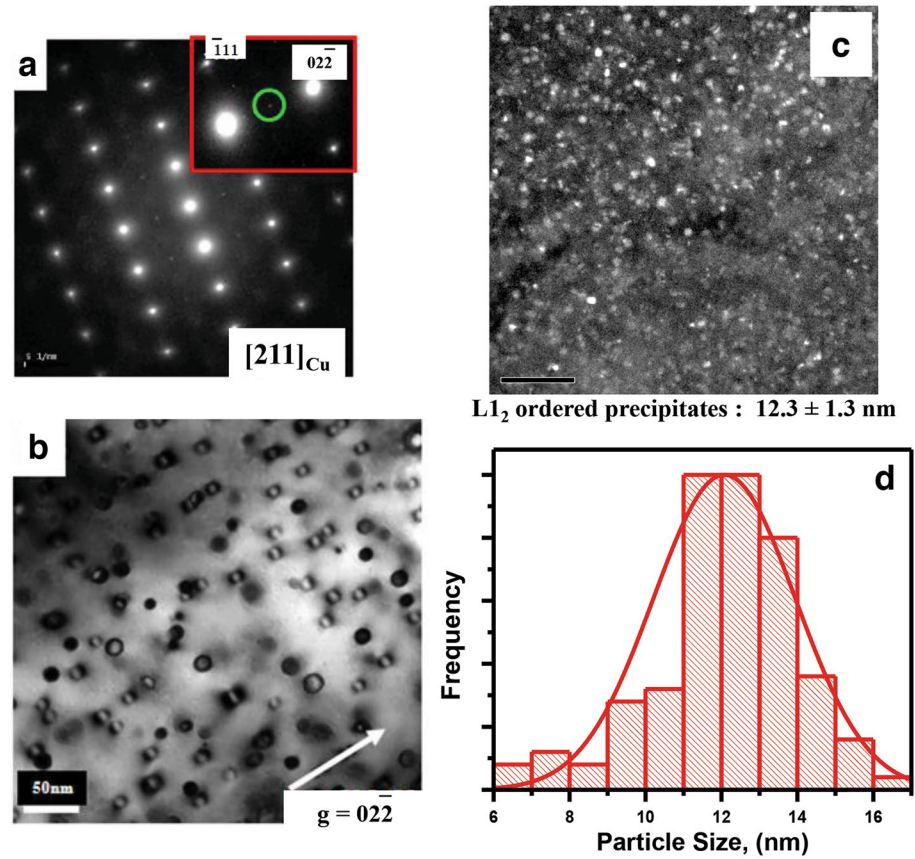


Fig. 4 (a) STEM HAADF images of $L1_2$ ordered precipitates in the continuous fcc copper matrix. (b)–(d) Elemental mapping using a STEM nanoprobe of the $L1_2$ ordered precipitates showing the nature of partitioning of Fe, Si, and Cu across the precipitate particles and the fcc copper matrix

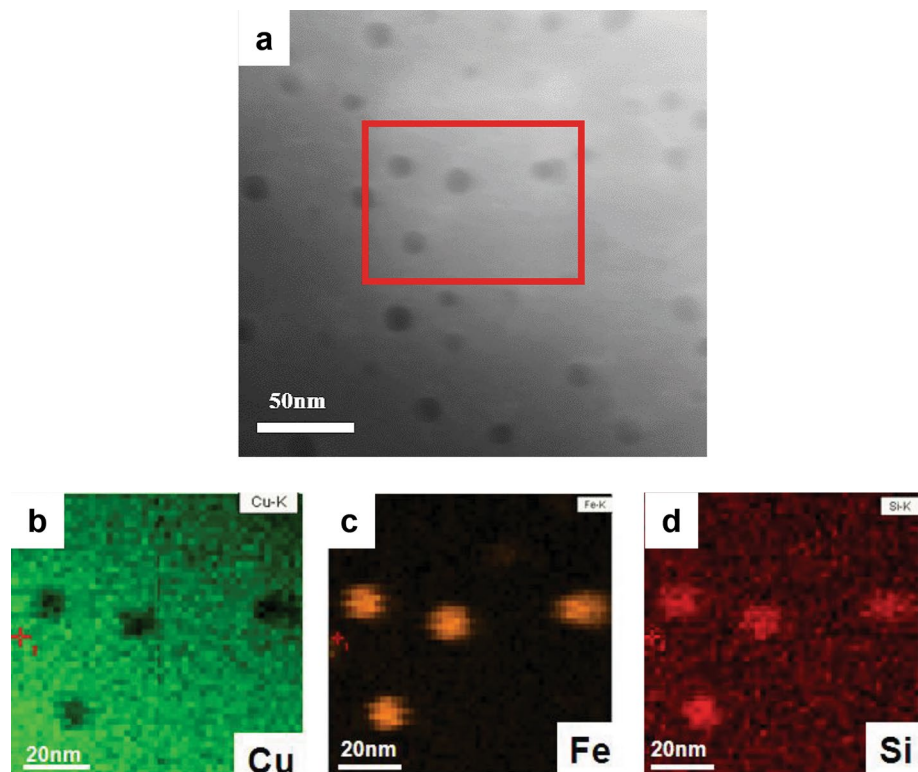


Figure 5a shows the 3D APT results of a suction cast sample showing the precipitates. The larger precipitates are revealed by the Fe24% isosurface containing Fe, Si and a small amount of Cu. These have sizes similar to the one observed by TEM in Figs. 3 and 4. The composition profile across one of these clusters is shown in Fig. 5b. The exact stoichiometry of the $L1_2$ ordered γ' particle is 9% Cu, 68% Fe, and 23% Si. In addition, we could also reveal a few early stages clustering (less than 5 nm size) by Fe-6at% isosurface of the elemental distributions.

The high-resolution phase contrast image of the $L1_2$ ordered precipitate taken along the [011] zone is shown in Fig. 6a. The FFT (Fast Fourier Transform) obtained from the region is presented in Fig. 6b which reveals the superlattice reflections. One can observe layers marked A and B with intensity variations, as shown as inset in the image (Fig. 6a). A model 011 projection of the $L1_2$ structure of A (Fe/Cu) and B(Si) atoms is shown in Fig. 6c. The periodic intensity variation can be qualitatively associated with the iron-rich and silicon-rich columns in the ABA type layer expected with the $L1_2$ ordering. A high-resolution phase contrast micrograph at the interface of the $L1_2$ ordered precipitate and Cu matrix, taken along the [011] matrix zone axis, is shown in Fig. 7a. The corresponding FFT patterns taken from the regions marked by (i) and (ii) separated by the interface are also shown in Fig. 7b and c, respectively.

These results provide the detailed information about the coherent nature of the interface between $L1_2$ ordered precipitate and the surrounding Cu-rich matrix. The FFT patterns confirm that the (100) plane of the $L1_2$ ordered precipitate (Red dotted circle in Fig. 7b) is parallel to the (200) plane of the Cu-matrix. This diffraction analysis and phase contrast high-resolution images confirm that these precipitates are $L1_2$ ordered and maintain a cube-on-cube orientation relationship with the copper rich fcc matrix. This coherent interface promotes a low interfacial energy between the $L1_2$ ordered precipitate particles and the copper matrix. This low interfacial energy helps in minimizing the driving force for coarsening at elevated temperature. This coarsening resistant property is important for maintaining the high temperature strength of the present alloy and can be noticed during heat treatment study.

To determine whether the precipitates retain their ordered structure, in situ heating experiments at different temperatures were carried out in TEM using the heating holder. The sample at each temperature was stabilized by holding 15 min before the diffraction experiment. Figure 8a–c shows a series of diffraction patterns as a function of temperature recorded under two-beam conditions along the [211] zone axis of copper. No significant changes in the diffraction patterns can be observed as the temperature

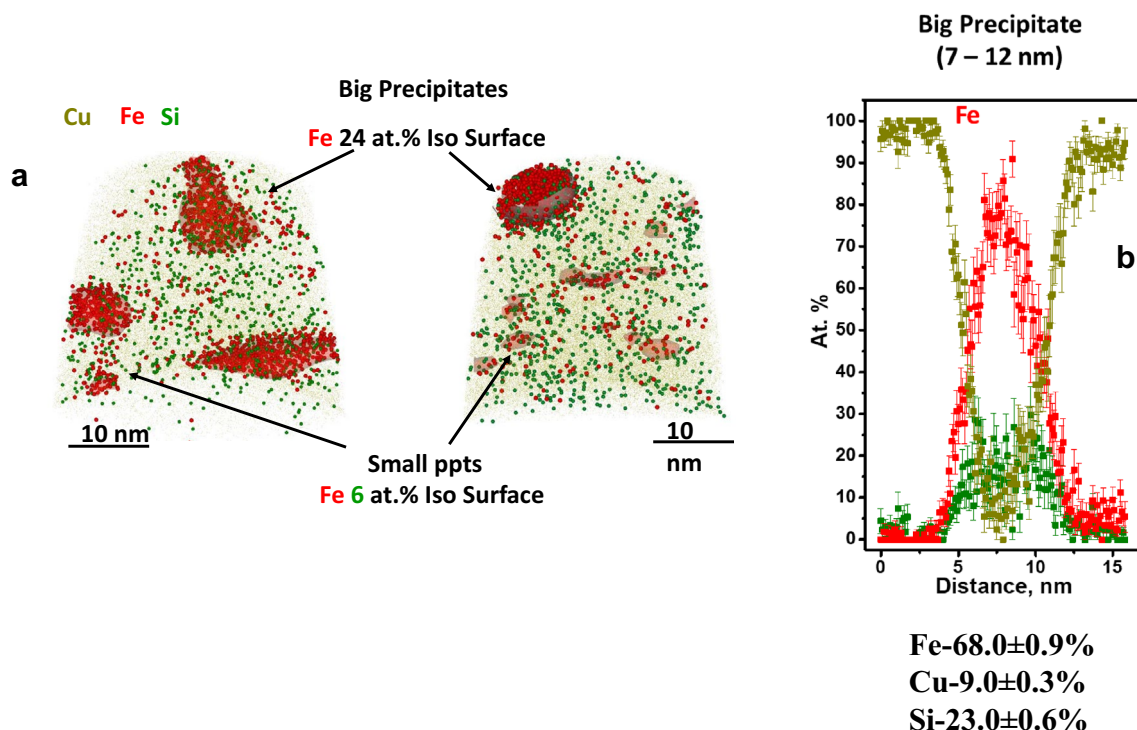


Fig. 5 (a) Section of the Atom probe tomographs of the suction cast alloy showing the distribution of the particles. (b) Atom probe concentration profile across the large particle showing the distribution of the Fe, Cu and Si atoms

“ABA” Layered Structure along [110] Projection

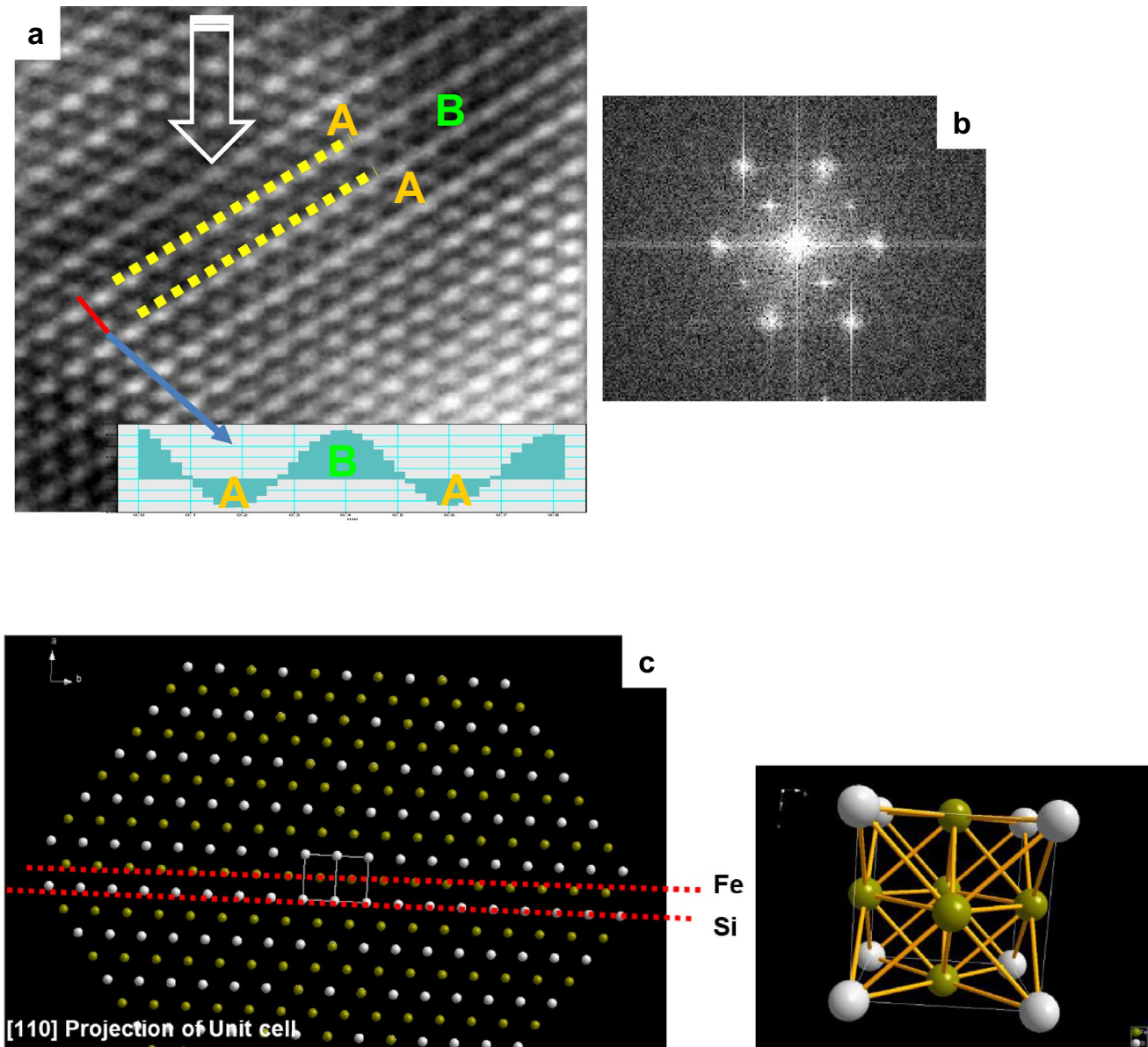


Fig. 6 (a) High-Resolution Phase Contrast TEM image showing the ordering of ABA type layers of Fe and Si with intensity variation among alternating ABA layer. Bottom image shows [110] projection of the model unit cell of the L₁₂ structure

increases from room temperature to 450 °C. It implies that the ordered structure is stable until this temperature.

The size of the particles remains similar even after 120 min of exposure till 450 °C. However, the size gets bigger when the samples were exposed isothermally at 600 °C for 120 min (Fig. 9a–c). The mean diameter of the L₁₂ ordered g' precipitates has increased from 12.3 ± 1.3 nm to 38.0 ± 4.4 nm during the isothermal exposure of 120 min (Fig. 9d). At 600 °C, the particles do not show any strain contrast when imaged under different two-beam conditions suggesting a loss of coherency strain at this temperature

[47–49]. However, superlattice spots are still visible in the diffraction patterns (Fig. 9a) indicating the presence of the ordering of the precipitates.

Mechanical Properties

Figure 10 displays the Vickers microhardness of the suction cast alloy as a function of time when held at an isothermal temperature of 400 °C. The lack of significant variation of the hardness with aging time suggests most of the precipitates formed during the cooling of the suction

Fig. 7 (a) High-Resolution phase contrast micrograph at the interface of the L1₂ ordered precipitate and copper matrix on the 011matrix zone axis. (b) and (c) corresponding FFT patterns. FFT patterns indicate the nature of the planes, (100) L1₂ ordered precipitate // (200) copper matrix

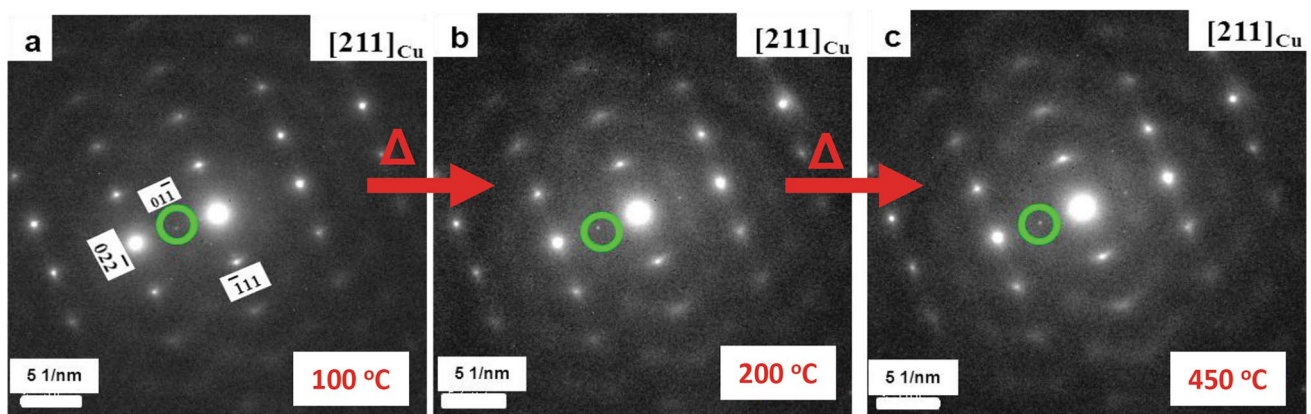
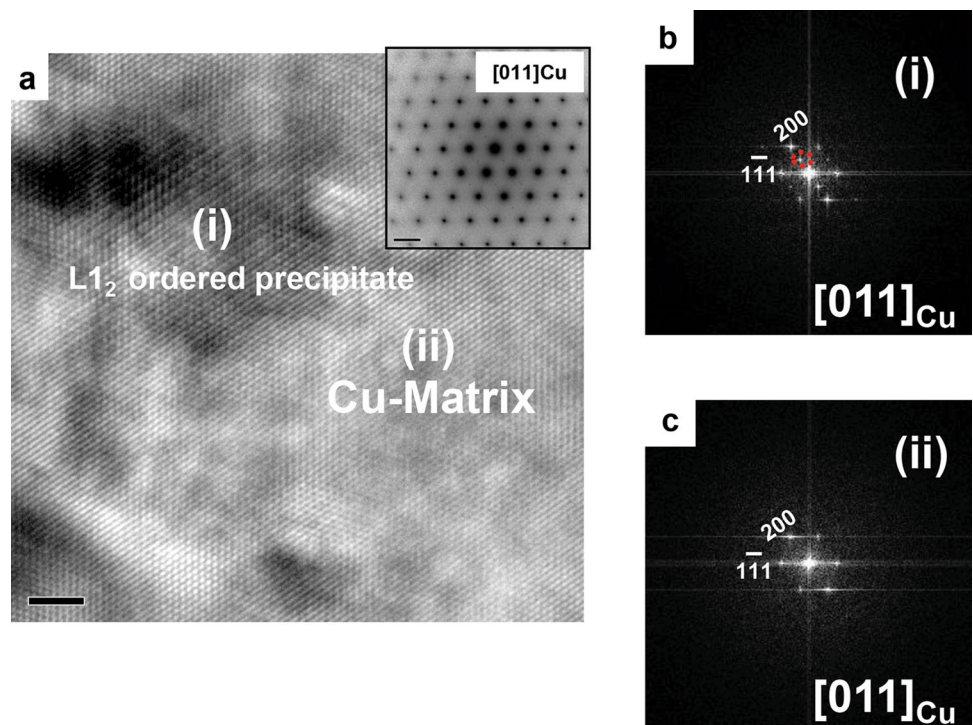


Fig. 8 (a)–(c) Series of diffraction patterns taken under 2-beam conditions along the [211] zone axis of copper matrix showing the in situ heating experiment in TEM

cast ingots. The mechanical properties of suction cast Cu-2.5at%Fe-2.5at% Si alloy are evaluated at room and elevated temperatures (400 and 600 °C). Miniature scale tensile samples were used to evaluate the mechanical properties, and sample details can be seen in the experimental section. Effects of sample size are an important function of the evolved bulk properties especially for the % elongation determination [67]. However, several studies showed that one can achieve a potential trend in the yield strength and ultimate tensile strength with a prescribed length to width ratio for different geometries of the tensile samples [67, 68]. In this present study, the trend in mechanical

behavior for the rapidly cast alloys was determined and projected in Fig. 11. Engineering stress vs engineering strain plots under tension at room temperature and different high temperatures (400 and 600 °C) are shown in Fig. 11a and b, respectively, as well as presented in Table 2. The room temperature yield strength of the alloy is 580 ± 18 MPa with $6 \pm 1.0\%$ elongation to failure. It is higher than other commercially and competitive Cu-base alloys [1–41]. High-temperature tensile test data further indicate that this alloy can retain a considerable amount of strength both at 400 °C (YS $\sim 320 \pm 11$ MPa) and at 600 °C (YS $\sim 128 \pm 8$ MPa).

Fig. 9 (a) SAD pattern taken along $[111]$ zone axis of copper matrix at $600\text{ }^{\circ}\text{C}$, aged for 120 min. (b) High-magnification bright field image of $L1_2$ ordered precipitates. (c) High-magnification dark field image of $L1_2$ ordered precipitates, showing absence of line of no contrast (coherency strain releasing). (d) Plot of mean particle diameter of $L1_2$ ordered precipitates as a function of aging temperature

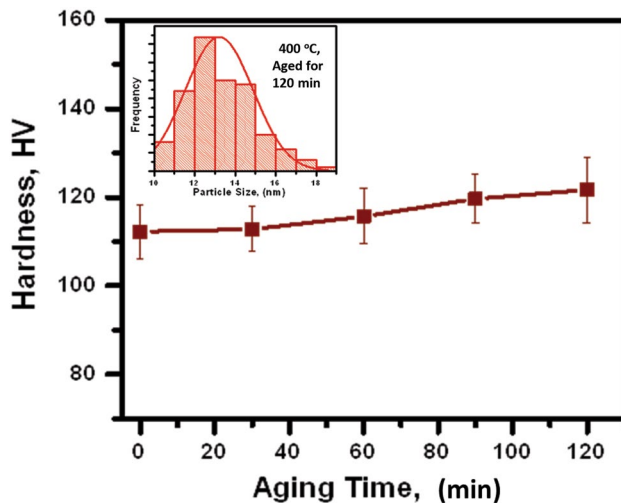
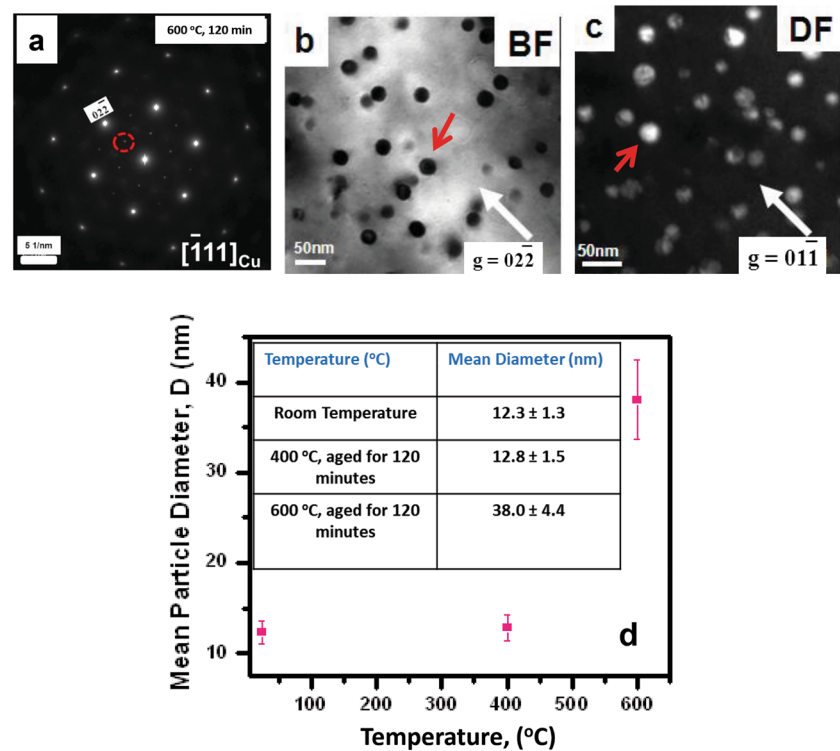


Fig. 10 Aging curve for the suction cast $\text{Cu-2.5at\%Fe-2.5at\%Si}$ alloy at $400\text{ }^{\circ}\text{C}$

Thermal Conductivity

The variation of total thermal conductivity with temperature for the alloy in the temperature range of $50\text{--}800\text{ }^{\circ}\text{C}$ is shown in Fig. 12a. The total thermal conductivity of the alloy monotonically increases with increasing temperature up to $700\text{ }^{\circ}\text{C}$. However, it drops beyond $800\text{ }^{\circ}\text{C}$. The observed increase in thermal conductivity with increasing temperature

makes the alloy attractive for high-heat flux applications. The alloy displays a thermal conductivity value of 313 (W/(mK)) at $600\text{ }^{\circ}\text{C}$, which is competitive with other copper base alloys [1–41]. Figure 12b shows the electronic and lattice contribution to the total thermal conductivity in the temperature range of $100\text{--}400\text{ }^{\circ}\text{C}$. The Wiedemann–Franz Law gives the electronic contribution (κ_e) [50, 51]. The lattice thermal conductivity κ_l can be computed by the relation, $\kappa_{\text{total}} = \kappa_e + \kappa_l$. Figure 12b confirms that the electronic contribution is dominant in the thermal conduction process for the current alloy in the temperature range of $100\text{--}400\text{ }^{\circ}\text{C}$.

The electronic part of thermal conductivity monotonically increases with increasing temperature, and the total thermal conductivity of the alloy follows the same trend as the electronic part. The increase in electronic contribution indicates that the impedance of the electronic flow has been minimized in the present alloy. The percentage ratio of electronic and lattice contribution to the total thermal conductivity for the alloy is shown in Fig. 12c. The result reveals that approximately 14% of heat conduction is contributed by phonon over the calculated temperature ranges. With increasing temperature, the percentage of phonon contribution decreases and the electronic part increases. The ordering of the precipitate also increases the thermal conductivity as ordering brings the alloy system close to a translationally invariant configuration, in which impurity scattering is minimized [51, 61]. Therefore, total thermal conductivity monotonically increases up to $700\text{ }^{\circ}\text{C}$ before dropping. The relaxation

Fig. 11 (a) Engineering stress vs engineering strain plot under tension at room temperature for the Cu-2.5at%Fe-2.5at% Si suction cast alloy. (b) Engineering stress vs engineering strain plot under tension at 400 and 600 °C for the Cu-2.5at%Fe-2.5at% Si suction cast alloy sample. (c) Design and schematic geometry of the tensile sample used in the present study

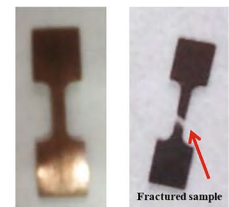
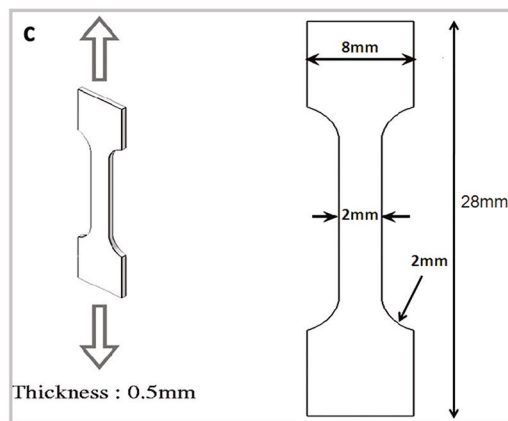
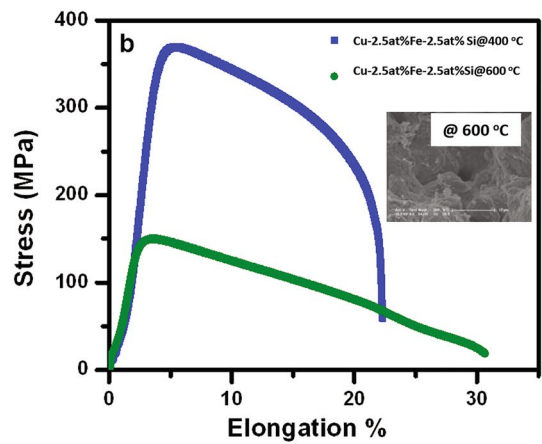
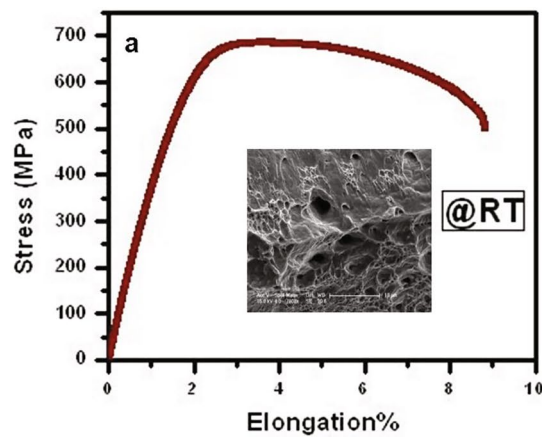


Table 2 Tensile properties for the Cu-2.5at%Fe-2.5at%Si suction cast alloy

Temperature, °C	Yield strength, MPa	UTS, MPa	%El
Room temperature	580 ± 18	690 ± 16	6 ± 1.0
400 °C	320 ± 11	370 ± 10	20 ± 2.0
600 °C	128 ± 8	150 ± 10	32 ± 1.0

of coherency strain with temperature reduces the electron scattering at the precipitate matrix interfaces. As an immediate consequence, the total thermal conductivity increases ($\rho(c, T) = \rho_0(c) + \rho_i(T)$), as $\rho_0(c)$ decreases and κ_e increases. However, lattice vibration increases with increasing temperature, and electron–phonon scattering also increases. The increased electron–phonon scattering enhances the system's intrinsic electrical resistivity (ρ_i) [66]. At some temperatures (~ 800 °C), this electron–phonon scattering dominates over the free electron movement in a partially strain-free matrix

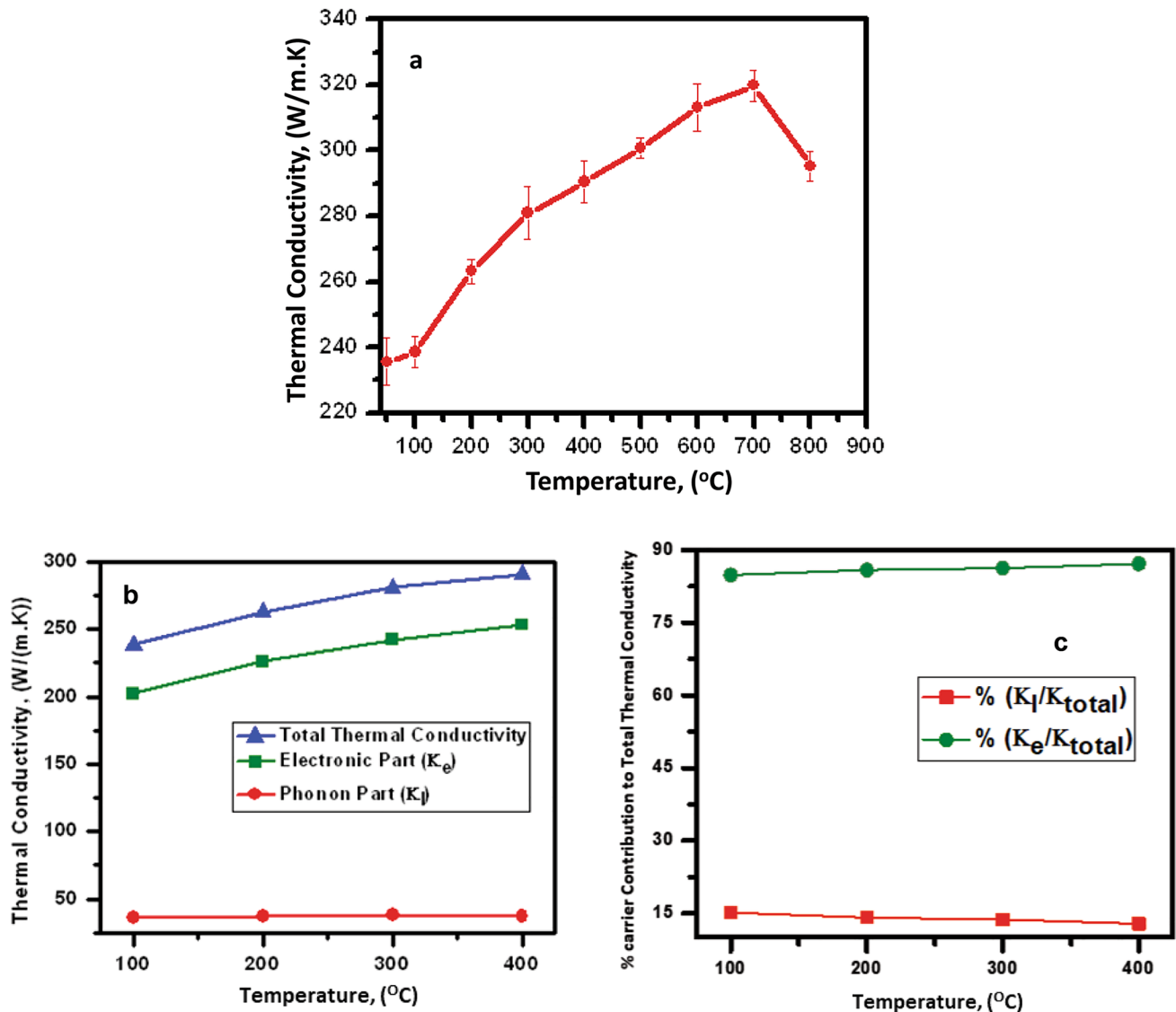


Fig. 12 (a) Total thermal conductivity plot as a function of temperature for the alloy. (b) Plot of electronic and lattice contribution to the total thermal conductivity Vs temperature for the alloy at the tem-

perature range of 100–400 °C. (c) Percentage ratio of electronic and lattice contribution to total thermal conductivity for the alloy at the temperature range of 100–400 °C

channel. As a result, total thermal conductivity again starts to decrease. This interplay between two terms of resistivity ($\rho_0(c)$ and $\rho_i(T)$) and their influence on κ_e plays an important role in heat conduction dynamics as κ_l is not a significant heat conductor for this alloy (Fig. 12b and c).

Discussion

Order Precipitates in Cast Cu-2.5Fe-2.5Si Alloy

The suction casting process can produce necessary undercooling to access the metastable miscibility gap in the Cu–Fe binary diagram. The present results on suction cast

Cu-2.5at%Fe-2.5at% Si alloy have established a new type of $L1_2$ ordered Fe–Si rich, coherent nanometer-sized γ' precipitates in the fcc γ copper matrix with a cube-on-cube orientation relationship.

Copper is immiscible with iron and exhibits a submerged miscibility gap (Fig. 13). The suction casting process can produce necessary undercooling to access this metastable miscibility gap. Novel metastable microstructures can be designed using a non-equilibrium solidification [15, 52]. However, our alloy composition most likely bypasses the submerged miscibility gap since the solubility of Si and Fe in copper at the melting temperature are nearly 8–11 at% Si and 2.1–2.4 at% Fe. Limited solid solubility of Cu in Fe exists at higher temperatures (dotted red box in Fig. 13).

Rapid solidification can kinetically trap some of the solutes in the matrix and yield a metastable supersaturated solid solution at a higher temperature that can decompose on further cooling during casting. The precipitation of fcc γ Fe phase (γ Fe) as a coherent GP zone instead of BCC α Fe in Cu-1.2%Fe alloy has been studied by Hono et al. [53]. Thus, according to the phase diagram, γ Fe is expected to disperse in the copper matrix during cooling. Once formed, the embedded γ Fe cannot easily transform to BCC α Fe since the space groups of these two crystal structures do not show a group subgroup relation [54]. The FCC/BCC interface, at best, shows partial coherency, and hence, energy cost of creating such an interface will be higher.

Silicon has a strong ordering tendency in iron lattice and forms ordered B2 structure [55–58]. The evolution of such an ordered structure is well studied [58]. The small amount of ternary silicon will promote its partition to both copper matrix and iron-rich precipitates. Consistent with Hono et al. [53], one expects the formation of precipitates of γ Fe containing Si stabilized by the surrounding fcc crystal field of the Cu matrix. The natural ordering tendency of silicon in iron and the demand for maintaining lattice coherency with the surrounding fcc copper matrix can lead to fcc-based $L1_2$ ordered coherent precipitate particles (γ') in the copper matrix. Thus, we have obtained a new type of $L1_2$ ordered coherent precipitate particles in the copper matrix instead of BCC ordered Fe_3Si structure. Our composition analysis also indicates the small presence of copper in the precipitate phase as copper has small solubility in iron at higher temperatures.

The lattice parameters from the X-ray analysis yield a negative misfit value (d) of -1.33% . A less accurate misfit

evaluated from FFTs obtained from high-resolution TEM images yields a negative misfit value $> 0.8\%$. The strong strain-field contrasts (with a line of no contrast under two-beam condition) confirm a large coherency strain associated with these particles originating from the misfit strain [59, 60]. Since Cu and Fe have a very similar lattice parameters, the strain originates primarily due to the ordering of Si with Fe in the γ' precipitates.

The nano-sized $L1_2$ ordered precipitates remain stable up to 450°C , as evidenced by the retention of the superlattice reflection in the diffraction pattern at different temperatures during the in situ heating experiments (Fig. 8). The very little change in the hardness values observed with time at 400°C also suggests little change in the average size. The isothermal holding of the sample at 600°C for 120 min also confirms the coherent $L1_2$ ordered structure (Fig. 9a). However, a threefold increase in the average diameter of the $L1_2$ ordered precipitates could be observed at 600°C (after 120 min of aging) (Fig. 9d). The lattice matching between the $L1_2$ ordered γ' and the surrounding copper-rich g matrix and cube-on-cube orientation relationship between ordered particles and the copper matrix promotes low interfacial energy between the $L1_2$ ordered precipitate particles and the surrounding copper matrix. It helps minimize the driving force for coarsening at elevated temperatures.

Origin of High-Temperature Mechanical Properties

The resistance to coarsening is important in the context of maintaining high-temperature strength. Although the average diameter of the $L1_2$ ordered γ' precipitates has increased three times at 600°C compared to room temperature, the increment (12.3 ± 1.3 nm to 38 ± 4.4 nm) still may not affect the high-temperature strength to a great extent.

Exposing the alloy for 120 min at 600°C leads to the disappearance of the line of no contrast or Ashby–Brown strain contrast (Fig. 9b, c) in both the bright field and dark field images. The absence of strain contrast indicates the release of coherency strain at the interface. However, the superlattice spots corresponding to $L1_2$ ordering are still present in the SAD patterns at this temperature. Thus, the alloy derives its mechanical strength from a combination of different mechanisms, including order hardening and coherency strengthening, and their relative contributions may depend on the temperature [62–65]. A combined plot showing the dynamics of precipitates growth and corresponding strengthening situation with respect to the evolved yield strength is presented in Fig. 14. This plot reflects that even in the loss of coherency strain, the alloy still draws strength through order hardening mechanism. The moving dislocation with its disordered repeat distance will always destroy the atomic order in the ordered structure. Therefore, a passing dislocation in an ordered structure needs to have larger Burgers vectors, l bl,

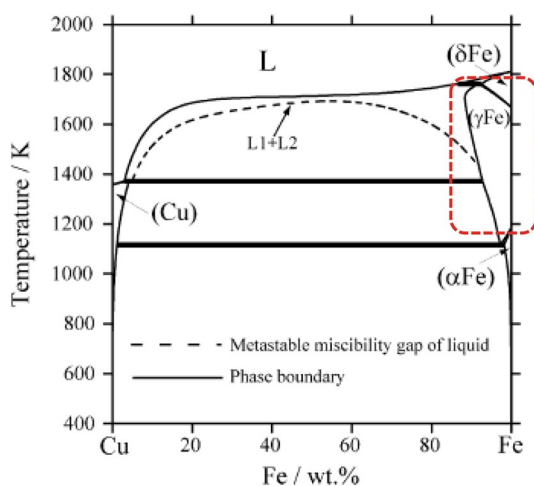


Fig. 13 Binary phase diagram of Cu–Fe system showing the existence of submerged miscibility gap¹³ and the γ Fe phase field (red dotted box) at high temperature, accessed by the process of phase separation during suction casting process of Cu-2.5at%Fe-2.5at% Si alloy

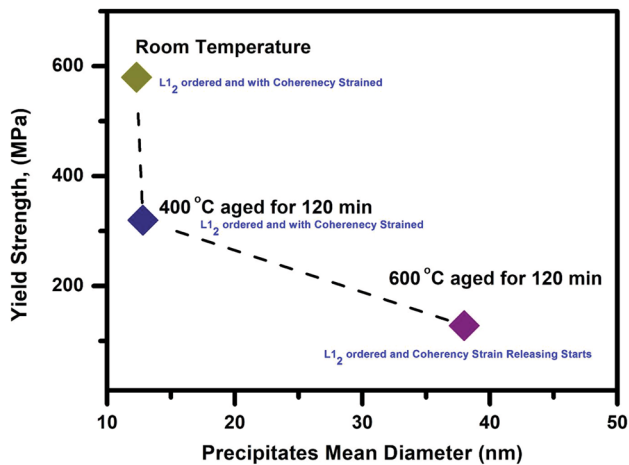


Fig. 14 A combined plot showing the dynamics of precipitates growth and corresponding strengthening situation with respect to the evolved yield strength

to restore the decrease in translation symmetry that occurs on ordering. A larger Burgers vector, $|\mathbf{b}|$ associated with the higher self-energy, is not energetically favorable to form and move. Thus, a pair of dislocations move with the first one destroying the order for a precipitate particle having an ordered structure. The second, trailing dislocation, restores the order, making the deformation process more complex [61, 62]. This kind of order hardening mechanism enhances the yield strength of the alloy.

Along with the order hardening, the contribution of coherency strain to the yield strength needs to be considered [62–65]. The increment in the yield strength of the alloy can be explained in terms of the developed internal stresses due to the misfit between the $L1_2$ ordered precipitates and the surrounding copper matrix. The misfit (ϵ), in this case, is 0.013 (1.3%). The enhanced yield strength, $\Delta\tau$, arising due to the coherency strain was theoretically calculated by Gerold and Haberkorn and further modified by Gleiter, Ham, and Brown [64, 65].

A comparison diagram of yield strength as a function of temperature of newly developed alloy along with other commercially important copper-based alloys is presented in Fig. 15 [1–41]. Figure 15 hints that the room temperature yield strength of Cu-2.5at%Fe-2.5at% Si alloy is greater than to the other existing copper alloys. The alloy with the brand name of AMZIRC and the Cu–Cr–Zr alloys displays a comparable high yield strength at room temperature. Figure 15 also shows that the evaluated yield strength of Cu-2.5at%Fe-2.5at% Si alloy at 600 °C can be compared with only Cu–Cr–Zr and NARloy-z alloys. The temperature dependent comparison diagram shows that the AMZIRC alloy has lost a greater extent of its yield strength at elevated temperatures. The comparison diagram clearly reflects that the yield strength of Cu-2.5at%Fe-2.5at% Si alloy at

600 °C is comparable to GRCop-84 and NARloy-z alloys. The yield strength and the thermal conductivity are sensitive functions of processing parameters. In the literature, variations in mechanical strength and conductivity values are reported for various alloy systems depending on the processing parameter. No special processing is introduced in the present work to enhance the mechanical properties. Thus, we have tried to extract only the as-cast data sets of various competitive copper-based alloy systems for comparison [1–41]. The strength-thermal conductivity plot of different alloys at 600 °C is displayed in Fig. 16. Therefore, it can be seen that the present alloy demonstrates excellent balance between strength and conductivity at elevated temperature. This inspiring trend of the developed alloy has the potential to find an attractive place with other copper-based alloys for high-temperature applications.

Conclusions

1. We have designed a copper-based alloy with γ - γ' microstructure in a Cu–Fe–Si system with coherent $L1_2$ ordered precipitates inside the continuous Cu-rich matrix by rapid solidification technique.
2. The $L1_2$ ordered γ' precipitates are rich in Fe and Si and coherent with a copper matrix with a cube-on-cube orientation relationship.
3. These $L1_2$ ordered precipitates are structurally stable at high temperatures.
4. Due to low interfacial energy with the surrounding copper matrix and decreased solubility of Fe due to miscibility gap, these ordered precipitates are coarsening resistant at high temperatures.

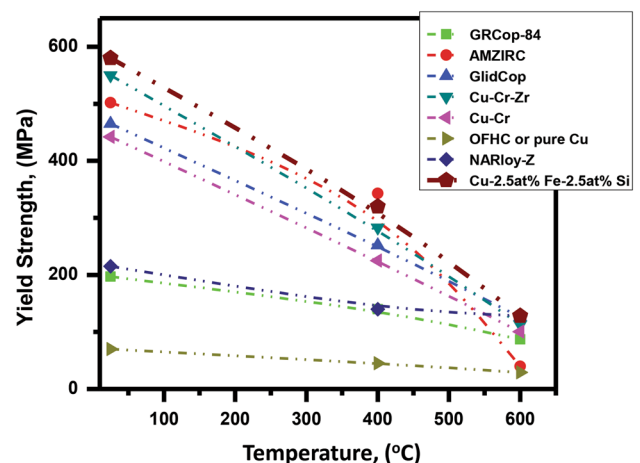


Fig. 15 Comparison of temperature dependent yield strength of newly developed Cu-2.5at%Fe-2.5at% Si suction cast alloy with other different important copper base alloys [1–30,55]

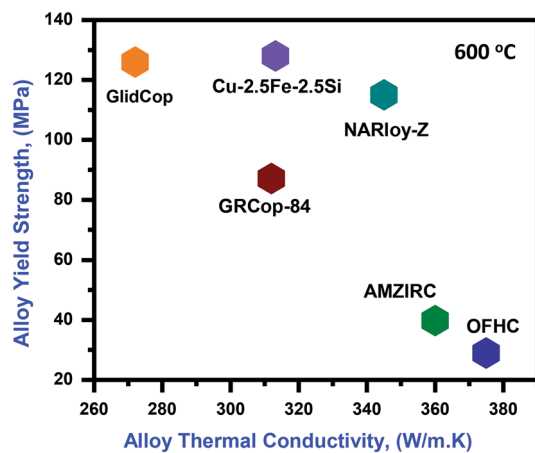


Fig. 16 Comparison of temperature dependent yield strength of newly developed Cu-2.5at%Fe-2.5at% Si suction cast alloy with other different important copper base alloys at 600 °C [13–20,55]

- The coherency strain associated with these $L1_2$ ordered precipitates and the ordered crystal structure contributes to its excellent mechanical strength at room temperature.
- The coherency strain vanishes at high temperatures, and order hardening is responsible for its high-temperature strength.
- The conductivity increases with temperature due to the vanishing of coherency strain till 700 °C. It makes the alloy a candidate for high-strength, high-conductivity applications at high temperatures.

Supplementary Information The online version contains supplementary material available at <https://doi.org/10.1007/s13632-023-00938-2>.

Acknowledgements The authors would like to acknowledge the funding from the STC (ISRO-IISc) grant from the Indian Institute of Science, Bangalore. The authors also acknowledge the facility available in the AFMM Centre in IISc.

Declarations

Conflict of interest The authors declare that they have no known competing financial interests or personal relationships that could have appeared to influence the work reported in this paper.

References

- M. Li, S.J. Zinkle, Physical and mechanical properties of copper and copper alloys. *Compr. Nucl. Mater.* **4**, 667–690 (2012)
- H.C. de Groh, D.L. Ellis, W.S. Loewenthal, Comparison of GRCop-84 to other Cu alloys with high thermal conductivities. *J. Mater. Eng. Perform.* **17**(4), 594 (2008)
- D.L. Ellis, GRCop-84: A High-Temperature Copper Alloy for High-Heat-Flux Applications. NASA/TM-2005-213566, 1–30 (2005).

- J.H. Sanders, P.S. Chen, S.J. Gentz, R.A. Parr, Microstructural investigation of the effects of oxygen exposure on NARloy-Z. *Mater. Sci. Eng. A.* **203**, 246–255 (1995)
- X. Zhang, Y. Zhang, B. Tian, K. Song, P. Liu, Y. Jia, X. Chen, J. An, Z. Zhao, Y. Liu, A.A. Volinsky, X. Li, T. Yin, Review of nano-phase effects in high strength and conductivity copper alloys. *Nanotechnol. Rev.* **8**, 383–395 (2019). <https://doi.org/10.1515/ntrev-2019-0034>
- R. Li, H. Kang, Z. Chen, G. Fan, C. Zou, W. Wang, S. Zhang, Y. Lu, J. Jie, Z. Cao, T. Li, T. Wang, A promising structure for fabricating high strength and high electrical conductivity copper alloys. *Sci. Rep.* **6**, 20799 (2016). <https://doi.org/10.1038/srep20799>
- Y. Pang, G. Chao, T. Luan, S. Gong, Y. Wang, Z. Jiang, Z. Xiao, Y. Jiang, Z. Li, Microstructure and properties of high strength, high conductivity and magnetic Cu–10Fe–0.4Si alloy. *Mater. Sci. Eng. A.* **826**, 142012 (2021). <https://doi.org/10.1016/j.msea.2021.142012>
- C. Zhang, C. Chen, X. Liu, M. Yan, M. Qi, X. Li, Y. Li, H. Zhang, F. Yang, W. Wang, Z. Guo, High strength and high electrical conductivity in Cu–Fe alloys with nano and micro-Fe particles. *Mater. Sci. Eng. A.* **855**, 143948 (2022). <https://doi.org/10.1016/j.msea.2022.143948>
- P. Zhanga, Q. Leia, X. Yuan, X. Sheng, D. Jiang, Y. Li, Z. Li, Microstructure and mechanical properties of a Cu–Fe–Nb alloy with a high product of the strength times the elongation. *Mater. Today Commun.* **25**, 101353 (2020). <https://doi.org/10.1016/j.mtcomm.2020.101353>
- K. Osipovich, A. Vorontsov, A. Chumaevskii, D. Gurianov, N. Shamarin, N. Savchenko, E. Kolubaev, Characterization of a bimetallic multilayered composite “stainless steel/copper” fabricated with wire-feed electron beam additive manufacturing. *Metals.* **11**, 1151 (2021). <https://doi.org/10.3390/met11081151>
- D. Stroz, T. Panek, H. Morawiec, Influence of the addition of a third element to the precipitation process in Cu–Fe alloys. *Mater. Sci. Eng.* **58**, 43–53 (1983)
- X.Y. Lu, C.D. Cao, B. Wei, Microstructure evolution of under-cooled iron-copper hypo-peritectic alloy. *Mater. Sci. Eng. A.* **313**, 198–206 (2001)
- C.P. Wang, X.J. Liu, M. Jiang, I. Ohnuma, R. Kainuma, K. Ishida, Thermodynamic database of the phase diagrams in copper base alloy systems. *J. Phys. Chem. Solids.* **66**, 256–260 (2005)
- S. Bysakh, K. Chattopadhyay, T. Maiwald, R. Galun, B.L. Mordike, Microstructure evolution in laser alloyed layer of Cu–Fe–Al–Si on Cu substrate. *Mater. Sci. Eng. A.* **375–377**, 661–665 (2004)
- S. Sarkar, C. Srivastava, K. Chattopadhyay, Development of a new class of high strength copper alloy using immiscibility route in Cu–Fe–Si system: Evolution of hierarchical multi-scale microstructure. *Mater. Sci. Eng. A.* **723**, 38–47 (2018)
- M. Wang, Y. Jiang, Z. Li, Z. Xiao, S. Gong, W. Qiu, Q. Lei, Microstructure evolution and deformation behaviour of Cu–10 wt.%Fe alloy during cold rolling. *Mater. Sci. Eng. A.* **801**, 140379 (2021)
- B. Jeong, H.R. Jo, J.T. Kim, S.H. Hong, K.B. Kim, A study on the micro-evolution of mechanical property and microstructures in (Cu–30Fe)–2X alloys with the addition of minor alloying elements. *J. Alloys Compd.* **786**, 341–345 (2019)
- S. Liu, S. Xu, J. Jie, J. Zhang, Y. Dong, X. Li, T. Li, Microstructure evolution and magnetic properties of metastable immiscible Cu–Fe alloy with micro-alloying B element. *J. Alloys Compd.* **888**, 161627 (2021)
- S. Liu, J. Jie, Z. Guo, S. Yue, T. Li, A comprehensive investigation on microstructure and magnetic properties of immiscible Cu–Fe alloys with variation of Fe content. *Mater. Chem. Phys.* **238**, 121909 (2019). <https://doi.org/10.1016/j.matchemphys.2019.121909>

20. D. Yuan, H. Zeng, X. Xiao, H. Wang, B. Han, B. Liu, B. Yang, Effect of Mg addition on Fe phase morphology, distribution and aging kinetics of Cu-65Fe alloy. *Mater. Sci. Eng. A.* **812**, 141064 (2021)
21. Y. Li, X. Yuan, B. Yang, X. Ye, P. Zhang, H. Lang, Q. Lei, J. Liu, Y. Li, Hierarchical microstructure and strengthening mechanism of Cu-36.8Fe alloy manufactured by selective laser melting. *J. Alloys Compd.* **895**, 162701 (2022)
22. A.J. Perry, Directionally solidified copper-CuZrSi pseudo-binary eutectic alloys. *Mater. Sci. Eng.* **11**, 203–209 (1973). [https://doi.org/10.1016/0025-5416\(73\)90079-7](https://doi.org/10.1016/0025-5416(73)90079-7)
23. A.J. Perry, A.R. Nicoll, K. Phillips, P.R. Sahm, The copper-boron eutectic-unidirectionally solidified. *J. Mater. Sci.* (1973). <https://doi.org/10.1007/BF00549350>
24. A.J. Perry, A.R. Nicoll, Properties of alloys on the tie-line between the copper-CuZrGe pseudo-binary eutectic and the copper-Cu5Zr eutectic. *J. Mater. Sci.* **8**, 883–892 (1973). <https://doi.org/10.1007/BF00553740>
25. C.S. Tiwary, P. Pandey, S. Sarkar, R. Das, S. Samal, K. Biswas, K. Chattopadhyay, Five decades of research on the development of eutectic as engineering materials. *Prog. Mater. Sci.* (2021). <https://doi.org/10.1016/j.pmatsci.2021.100793>
26. J.R. Davis, ASM specialty handbook: copper and copper alloys. ASM International. Materials Park, OH, p 276 (2001).
27. H.C. de Groh III, D.L. Ellis, W.S. Loewenthal, Comparison of GRCop-84 to other high thermal conductive Cu alloys. NASA/TM-2007-214663 (2007).
28. D.L. Ellis, G.M. Michal, Mechanical and thermal properties of two Cu–Cr–Nb alloys and NARloy-Z. NASA Contractor Report 198529 (1996).
29. K.R. Anderson, J.R. Groza, Microstructural size effects in high-strength high-conductivity Cu–Cr–Nb alloys. *Metall. Mater. Trans. A.* **32A**, 1211 (1996)
30. H.C. de Groh III, D.L. Ellis, W.S. Loewenthal, Comparison of AMZIRC and GRCop-84. *Mat. Sci & Tech. 2005 Conf & Exhb.* ASM/TMS, Pittsburg, PA (2005).
31. J.J. Stephens, D.T. Schmale, The effect of high temperature braze thermal cycles on mechanical properties of a dispersion strengthened copper alloy. *SAND87-1296. UC-20*, (1987), 1988 second printing.
32. Y. Wang, M. Chen, F. Zhou, E. Ma, High tensile ductility in a nanostructured metal. *Nature.* **419**(6910), 912–915 (2002). <https://doi.org/10.1038/nature01133>
33. L. Lu, Y. Shen, X. Chen, L. Qian, K. Lu, Ultrahigh strength and high electrical conductivity in copper. *Science.* **304**(5669), 422–426 (2004). <https://doi.org/10.1126/science.1092905>
34. L. Lu, X. Chen, X. Huang, K. Lu, Revealing the maximum strength in nanotwinned copper. *Science.* **323**(5914), 607–610 (2009). <https://doi.org/10.1126/science.1167641>
35. X. Li, Y. Wei, L. Lu, K. Lu, H. Gao, Dislocation nucleation governed softening and maximum strength in nano-twinned metals. *Nature.* **464**(7290), 877–880 (2010). <https://doi.org/10.1038/nature08929>
36. H. Sun, H.G. Wheat, Corrosion study of Al₂O₃ dispersion strengthened Cu metal matrix composites in NaCl solutions. *J. Mater. Sci.* **28**, 5435–5442 (1993)
37. S.-Y. Chang, S.-J. Lin, Fabrication of SiC_w reinforced copper matrix composite by electroless copper plating. *Scripta Mater.* **35**(2), 225–231 (1996)
38. S.C. Tjong, K.C. Lau, Tribological behaviour of SiC particle-reinforced copper matrix composites. *Mater. Lett.* **43**(5–6), 274–280 (2000)
39. K. Maki, Y. Ito, H. Matsunaga, H. Mori, Solid-solution copper alloys with high strength and high electrical conductivity. *Scripta Mater.* **68**, 777–780 (2013)
40. W. Bonfield, B.C. Edwards, Precipitation hardening in Cu 1.81 wt % Be 0.28 wt % Co. *J. Mater. Sci.* **9**, 415–422 (1974)
41. S. Nagarjuna, K.K. Sharma, I. Sudhakar, D. Sarma, Age hardening studies in a Cu–4.5Ti–0.5Co alloy. *Mater. Sci. Eng. A.* **313**(1–2), 251–260 (2001)
42. K. Thompson, D. Lawrence, D.J. Larson, J.D. Olson, T.F. Kelly, B. Gormanb, In situ site-specific specimen preparation for atom probe tomography. *Ultramicroscopy.* **107**, 131–139 (2007)
43. S.K. Makineni, M. Lenz, P. Kontis, Z. Li, A. Kumar, P.J. Felfer, S. Neumeier, M. Herbig, E. Spiecker, D. Raabe, B. Gault, Correlative microscopy—novel methods and their applications to explore 3D Chemistry and structure of nanoscale lattice defects: a case study in superalloys. *JOM.* **70**, 1736–1743 (2018)
44. M.F. Ashby, L.M. Brown, Diffraction contrast from spherically symmetrical coherency strains. *Philos. Mag.* **8**, 1083 (1963)
45. K.G. McIntyre, M.L. Brown, *J. Phys.* **27**, C3178 (1966)
46. S. Matsumura, M. Toyohara, Y. Tomokiyos, Strain Contrast of Coherent Precipitates in bright-field images under zone axis incidence. *Philos. Mag. A.* **62**(6), 653–670 (1990)
47. K.E. Knipling, D.C. Dunand, D.N. Seidman, Precipitation evolution in Al–Zr and Al–Zr–Ti alloys during isothermal aging at 375–425 °C. *Acta Mater.* **56**, 114–127 (2008)
48. C. Watanabe, D. Watanabe, R. Monzen, Coarsening behavior of Al₃Sc precipitates in an Al–Mg–Sc alloy. *Mater. Trans.* **47**(9), 2285–2291 (2006)
49. M. Nemoto, N. Morishige, T. Oguchi, H. Suto, The loss of coherency of θ' precipitates in an aluminum-copper alloy. *Trans. JIM.* **12**, 429 (1971)
50. R. Franz, G. Wiedemann, Ueber die Wärme-Leitungsfähigkeit der Metalle. *Ann. Phys.* **165**(8), 497–531 (1853)
51. J. Banhart, G. Czycholl, Electrical conductivity of long-range-ordered alloys. *Europhys. Lett.* **58**(2), 264–270 (2002)
52. P. Pawlik, K. Pawlik, A. Przyby, Investigation of the cooling rate in the suction casting process. *Rev. Adv. Mater. Sci.* **18**, 81–84 (2008)
53. K. Hono, H.W. Pickering, T. Sakurai, Atom probe analysis of γ iron precipitates in Cu-1.2at%Fe alloys. *Scripta Metall.* **22**, 881 (1988)
54. J.W. Cahn, G.M. Kalonji, Symmetry in solid-solid transformation morphologies, in *Proceedings of an International Conference Solid-solid Phase Transformations*. ed. by H.I. Aaronson, D.E. Laughlin, R.F. Sekerka, C.M. Wayman (AIME Press, New York, 1982), pp.3–15
55. F. Gonzalez, Y. Houbaert, A review of ordering phenomena in iron-silicon alloys. *Rev. Metal.* **49**(3), 178–199 (2013)
56. Z.Q. Gao, B. Fultz, Kinetics of ordering in Fe₃Si. *Hyperfine Interact.* **94**, 2361–2366 (1994)
57. V.P. Fadin, Y.A. Khon, V.E. Panin, Theory of ordering in ternary alloys with face-centered-cubic lattices. *Izvestiya VUZ. Fizika.* **11**(12), 71–79 (1968)
58. K. Raviprasad, K. Chattopadhyay, The influence of critical points and structure and microstructural evolution in iron-rich FeSi alloys. *Acta Metall. Mater.* **41**(2), 609–624 (1993)
59. H. Lee, S.Z. Han, H.M. Lee, Z.-H. Lee, Coarsening behavior of L1₂ precipitates in melt-spun Al–Ti–V–Zr alloys. *Mater. Sci. Eng. A.* **163**, 81–90 (1993)
60. H.M. Lee, J. Lee, Z.-H. Lee, Lattice misfit variation of Al₃(Ti, V, Zr) in Al–Ti–V–Zr alloys. *Scripta Metall. Mater.* **25**, 517–520 (1991)
61. D.E. Laughlin, Long-Range Order in Alloys, in *Encyclopedia of Materials Science and Engineering*, vol 1, (Pergamon Press, Oxford, 1938), pp.263–268
62. R.J. Grylls, C.D.S. Tuck, M.H. Loretto, Strengthening of a cupronickel alloy by an ordered L1₂ phase. *Intermetallics.* **4**, 567–570 (1996)

63. K. Matsuura, M. Kitamura, K. Watanabe, The precipitation hardening of Cu–Fe alloy single crystals with coherent γ -iron particles. *Trans. JIM.* **19**, 53 (1978)
64. V. Gerold, H. Haberkorn, On the critical resolved shear stress of solid solutions containing coherent precipitates. *Phys. Status Solidi.* **16**(2), 675–684 (1966)
65. H. Gleiter, *Z. Angew. Physik.* **23**, 108 (1967)
66. A. Matthiessen, 'Notizuber die elektrische leitungsfahigkeit des goldes.' *Ann. Phys.* **109**, 526–528 (1860)
67. M.S. Masete, N.S. Muchavi, S. Chikosha, The effect of specimen geometry on tensile properties of titanium alloy metal sheet. *IOP Conf. Ser. Mater. Sci. Eng.* **430**, 012015 (2018). <https://doi.org/10.1088/1757-899X/430/1/012015>
68. G.B. Rathmayr, A. Bachmaier, R. Pippan, Development of a new testing procedure for performing tensile tests on specimens with

sub-millimetre dimensions. *J. Test. Eval.* **41**(4), 1–12 (2013). <https://doi.org/10.1520/JTE20120175>

Publisher's Note Springer Nature remains neutral with regard to jurisdictional claims in published maps and institutional affiliations.

Springer Nature or its licensor (e.g. a society or other partner) holds exclusive rights to this article under a publishing agreement with the author(s) or other rightsholder(s); author self-archiving of the accepted manuscript version of this article is solely governed by the terms of such publishing agreement and applicable law.